



UNIVERSITY OF LEEDS

This is a repository copy of *Rapid solidification morphologies in Ni<sub>3</sub>Ge: Spherulites, dendrites and dense-branched fractal structures*.

White Rose Research Online URL for this paper:  
<http://eprints.whiterose.ac.uk/102460/>

Version: Accepted Version

---

**Article:**

Haque, N, Cochrane, RF and Mullis, AM (2016) Rapid solidification morphologies in Ni<sub>3</sub>Ge: Spherulites, dendrites and dense-branched fractal structures. *Intermetallics*, 76. pp. 70-77. ISSN 0966-9795

<https://doi.org/10.1016/j.intermet.2016.06.012>

---

© 2016, Elsevier. Licensed under the Creative Commons Attribution-NonCommercial-NoDerivatives 4.0 International  
<http://creativecommons.org/licenses/by-nc-nd/4.0/>

**Reuse**

Unless indicated otherwise, fulltext items are protected by copyright with all rights reserved. The copyright exception in section 29 of the Copyright, Designs and Patents Act 1988 allows the making of a single copy solely for the purpose of non-commercial research or private study within the limits of fair dealing. The publisher or other rights-holder may allow further reproduction and re-use of this version - refer to the White Rose Research Online record for this item. Where records identify the publisher as the copyright holder, users can verify any specific terms of use on the publisher's website.

**Takedown**

If you consider content in White Rose Research Online to be in breach of UK law, please notify us by emailing [eprints@whiterose.ac.uk](mailto:eprints@whiterose.ac.uk) including the URL of the record and the reason for the withdrawal request.



[eprints@whiterose.ac.uk](mailto:eprints@whiterose.ac.uk)  
<https://eprints.whiterose.ac.uk/>

# Rapid Solidification Morphologies in Ni<sub>3</sub>Ge: Spherulites, Dendrites and Dense-Branched Fractal Structures

*Nafisul Haque, Robert F. Cochrane and Andrew M Mullis*

Institute for Materials Research, University of Leeds, Leeds LS2 9JT UK.

## *Abstract*

Single-phase  $\beta$ -Ni<sub>3</sub>Ge has been rapidly solidified via drop-tube processing. At low cooling rates (850 – 300  $\mu\text{m}$  diameter particles, 700 – 2800  $\text{K s}^{-1}$ ) the dominant solidification morphology, revealed after etching, is that of isolated spherulites in an otherwise featureless matrix. At higher cooling rates (300 – 75  $\mu\text{m}$  diameter particles, 2800 – 25000  $\text{K s}^{-1}$ ) the dominant solidification morphology is that of dendrites, again imbedded within a featureless matrix. As the cooling rate increases towards the higher end of this range the dendrites display non-orthogonal side-branching and tip splitting. At the highest cooling rates studied (< 75  $\mu\text{m}$  diameter particles, > 25000  $\text{K s}^{-1}$ ), dense-branched fractal structures are observed. Selected area diffraction analysis in the TEM reveals the spherulites and dendrites are a disordered variant of  $\beta$ -Ni<sub>3</sub>Ge, whilst the featureless matrix is the ordered variant of the same compound. We postulate that the spherulites and dendrites are the rapid solidification morphology and that the ordered, featureless matrix grew more slowly post-recalescence. Spherulites are most likely the result of kinetically limited growth, switching to thermal dendrites as the growth velocity increases. It is extremely uncommon to observe such a wide range of morphologies as a function of cooling rate in a single material.

## **Introduction**

Chemically ordered intermetallic compounds have attracted considerable interest due to their potential application as high temperature structural materials resulting from their good chemical stability and high hardness at elevated temperatures. However, poor room temperature ductility limits their formability which has restricted industrial uptake of these materials. One route to increasing low temperature ductility is rapid solidification processing, wherein rapid crystallization results in a reduction of the degree of chemical ordering. Reordering of the material immediately following crystallization results in fine pattern of antiphase domains (APD's) which gives rise to increased ductility [1-3]. Importantly, the high temperature properties of the intermetallic can be restored by chemical ordering via annealing out the APD's subsequent to forming [1]. As such, understanding the process of disorder trapping and the morphology of the disordered regions following rapid solidification processing is critical to the increased uptake of intermetallics in high temperature structural applications.

APD's result from the transformation of the disordered solid to the ordered form via a nucleation process, with atom locations within a given nucleus being sublattice specific such that ordering between neighbouring nuclei is different [4]. Moreover, the morphology of the APD's formed during rapid solidification depends heavily upon the cooling rate of the solid

following growth [5]. For modest cooling rates columnar APD's are formed. At higher cooling rates equiaxed APD's can be formed while at very high cooling rates all reordering is suppressed.

For a given system we can define a critical temperature,  $T_C$ , at which the free energies of the ordered and disordered solid phases are equal. For the case in which  $T_C/T_M < 1$  (with  $T_M$  being the melting temperature) equilibrium growth of the solid will initially occur in the disordered state, with a subsequent disorder-order transformation occurring in the solid-state as the temperature drops below  $T_C$ . Conversely, if  $T_C/T_M > 1$ , equilibrium growth to the ordered solid phase will occur directly from the liquid. It is in such cases that rapid solidification can result in disordered growth as a consequence of the high growth rate, a phenomenon termed disorder trapping. Disorder trapping may be considered analogous to the more familiar process of solute trapping, wherein a non-equilibrium solute distribution occurs at the solid-liquid interface due to rapid solidification [6]. The extent of disorder trapping may be measured via the Long-Range Order (LRO) parameter,  $\eta$ , where  $\eta = 1$  represents the fully ordered intermetallic and  $\eta = 0$  is a random solid-solution.

In studying the effect of disorder trapping within intermetallics, congruently melting compounds are particularly attractive as, even during equilibrium solidification, a melt at the correct stoichiometry for the compound will solidify without partitioning. Disorder trapping may therefore be studied without the complication of considering simultaneous solute trapping. For such a congruently melting compound  $\eta$  will decrease with increasing solidification velocity as progressively higher levels of chemical disorder are trapped in the structure [7]. In a second order transition  $\eta$  falls continuously with increasing growth velocity, approaching zero at sufficiently high velocity. Conversely, in a first order transition,  $\eta$  decreases continuously from its equilibrium value, until a critical velocity,  $V_C$ , is reached, above which  $\eta$  drops discontinuously to zero.

It has been demonstrated in a range of intermetallic systems (see e.g. [8] in relation to the B2 AlNi phase, and [9] in relation to CoSi) that growth of the ordered phase is significantly slower than that of the disordered phase, with a jump in the growth velocity being evident at the (1<sup>st</sup> order) disorder-order transition. In a previous paper Ahmed *et al.* [10] studied disorder trapping in the congruently melting compound  $\beta$ -Ni<sub>3</sub>Ge using a flux undercooling technique. Unlike most other ordered intermetallics that have been subject to rapid solidification studies,  $\beta$ -Ni<sub>3</sub>Ge shares the L1<sub>2</sub> crystal structure with the important high temperature materials Ni<sub>3</sub>Al and Ti<sub>3</sub>Al. A maximum undercooling of 362 K was observed for  $\beta$ -Ni<sub>3</sub>Ge, wherein the corresponding growth velocity was measured at 3.55 m s<sup>-1</sup>. In common with other researchers who have determined the velocity-undercooling curves for intermetallic compounds passing through the order-disorder transformation, [10] observed a discontinuous break in the curve at the onset of fully disordered growth. This condition was observed for  $\beta$ -Ni<sub>3</sub>Ge at an undercooling of 168 K and at a critical growth velocity of 0.22 m s<sup>-1</sup>. This compares with  $V_C = 0.75$  m s<sup>-1</sup> in Fe-18 at.% Ge [11] and  $V_C = 3.8$  m s<sup>-1</sup> in CoSi [9]. Microstructural analysis of the  $\beta$ -Ni<sub>3</sub>Ge system [10] revealed a transition from a coarse grained structure during ordered growth to a much finer grained structure once disordered growth was achieved. However, post-recalescence cooling is very slow in flux undercooling experiments ( $\sim 10$  K s<sup>-1</sup>), meaning that any microstructural evidence of disorder

trapping will have been extensively modified in the as-solidified sample, with no prospect of observing either APD's or retained disordered material.

Other closely related intermetallic systems include  $\text{Fe}_3\text{Ge}$  and  $\beta\text{-Ni}_3\text{Si}$ .  $\text{Fe}_3\text{Ge}$  has an ordered hexagonal  $\text{D0}_{19}$  structure and so cannot be considered directly analogous to  $\beta\text{-Ni}_3\text{Ge}$ . It forms via the peritectic reaction  $\text{L} + \alpha_2 \rightarrow \epsilon$ , where  $\alpha_2$  is an ordered B2 phase, although for undercoolings in excess of 140 K direct solidification to the  $\epsilon$  phase should be possible. However, no evidence of an order-disorder transformation was observed at undercoolings up to 198 K, wherein the growth velocity was measured at  $1.3 \text{ m s}^{-1}$ . Conversely, one of the three  $\beta\text{-Ni}_3\text{Si}$  polymorphs does have the ordered fcc  $\text{L}_{12}$  crystal structure. However, while the phase diagram suggests single phase growth of  $\beta\text{-Ni}_3\text{Si}$  from the Ni-25at.% Si melt should be possible for undercoolings in excess of 43 K, both flux undercooling [12] and drop-tube studies [13] have revealed that such direct growth of  $\beta$  from the melt appears to be inhibited at all undercoolings in favour of a  $\alpha\text{Ni}-\gamma$  eutectic,  $\gamma$  being the phase  $\text{Ni}_{31}\text{Si}_{12}$ .

In this article we present an analysis of rapidly solidified Ni-23.8 at. % Ge produced using the drop-tube technique. Depending upon particle size, cooling rates in the drop-tube vary from  $700\text{-}50,000 \text{ K s}^{-1}$ , giving much greater scope than the work of [10] to retain disorder trapping and APD's in the as-solidified microstructure. As such the main objective of this work is to study the morphology of any retained regions of the disordered solid together with that of any APD's formed during post-recalcescence reordering in a single-phase system that acts as a simple model for high temperature  $\text{L}_{12}$  intermetallics.

## Experimental Method

According to the phase diagram of Nash and Nash [14], the Ni-rich portion of which is shown in Figure 1,  $\beta\text{-Ni}_3\text{Ge}$  is a congruently melting compound with a melting point of 1405 K. It has a homogeneity range of 22.5 to 25 at. % Ge and crystallizes to the ordered fcc  $\text{L}_{12}$  structure.

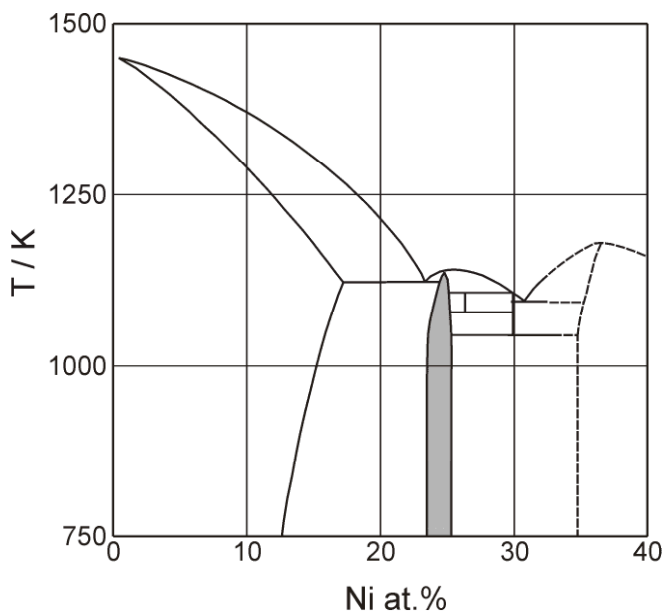


**Figure 1.** Ni-rich portion of the Ni-Ge phase diagram (based upon that of [14]), with the  $\beta$ -Ni<sub>3</sub>Ge phase shown shaded.

Elemental Ni and Ge were obtained from Alfa Aesar with purity of 99.99 % and 99.999%, metals basis, respectively. The alloy, of composition Ni-23.8 at. % Ge, was produced by arc-melting the elemental constituents together under a protective argon atmosphere at a pressure of  $5 \times 10^{-4}$  Pa before back-filling with argon gas to a pressure of  $3.4 \times 10^3$  Pa. A 230 A arc was produced using a tungsten electrode. The material was melted by manipulating the electrode above the sample, a process that was repeated 8 times to ensure uniform mixing of the final alloy. The final alloy was weighed following arc-melting to ensure there was no loss of material.

Following arc-melting the alloy ingot was sectioned using a Struers Accutom diamond precision saw and its phase composition checked using a PANalytical Xpert Pro X-ray diffractometer (XRD). The sectioned ingot was then mounted in transoptic resin using a Buehler Simplimet 1000 Automatic mounting press before being ground using progressively finer Silicon carbide grinding paper. The sample was then prepared for microstructural analysis by polishing with 6  $\mu\text{m}$ , 3  $\mu\text{m}$  and 1  $\mu\text{m}$  diamond paste, with the sample being washed and dried between each polishing step. The sample was then etched using Nital before being subject to microstructural analysis using an Olympus BX51 optical microscopy (OM) and a Carl Zeiss EVO MA15 scanning electron microscopy (SEM) equipped with X-Max Oxford instrument Energy-Dispersive X-Ray (EDX) detector.

If the alloy ingot were to show local deviations from single phase, due for instance to incomplete mixing of the elemental constituents during arc-melting, this would be apparent from the formation of fine eutectic structures at the boundaries of the Ni<sub>3</sub>Ge grains. On the Ni-rich side of the Ni<sub>3</sub>Ge compound this will be a Ni-Ni<sub>3</sub>Ge eutectic, whereas on the Ge-rich side this will be a eutectic between the Ni<sub>3</sub>Ge compound and either the Ni<sub>5</sub>Ge<sub>3</sub> or Ni<sub>2</sub>Ge compounds. Only once no evidence of intergranular eutectic following nital etching, nor of any phases other than Ni<sub>3</sub>Ge in the XRD analysis, were observed was the alloy deemed suitable for rapid solidification processing.

Rapid solidification was affected by drop-tube processing, using a 6.5 m drop-tube (see Figure 2). The tube was rough pumped to a pressure of  $2 \times 10^{-4}$  Pa before being flushed with N<sub>2</sub> gas. The rough pump – flush cycle was repeated three times before the tube was evacuated to a pressure of  $4 \times 10^{-7}$  Pa using a turbo-molecular pump. For sample processing the tube was filled with dried, oxygen free N<sub>2</sub> gas at a pressure of 50 kPa. The alloy sample, of approximately 9.5 g mass was loaded into an alumina crucible which has three 300  $\mu\text{m}$  laser drilled holes in the base. Induction of heating of a graphite subsector was used for heating the sample. Temperature determination was by means of an R-type thermocouple which sits inside the melt crucible, just above the level of the melt. When the temperature in the crucible attained 1480 K (75 K superheat) the melt was ejected by pressuring the crucible with  $\sim 400$  kPa of N<sub>2</sub> gas. This produces a fine spray of droplets which subsequently solidify in-flight and are collected at the base of the tube.

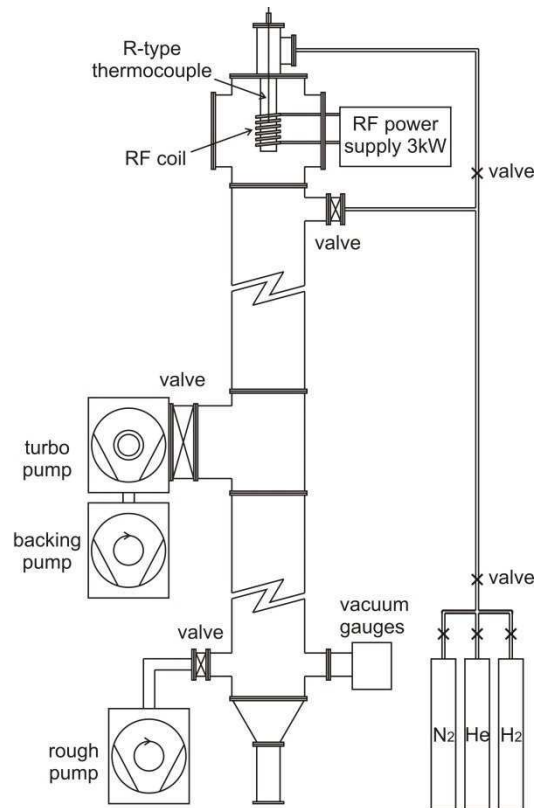


**Figure 2:** Schematic diagram of the drop-tube apparatus used in this study

The sample was weighed following removal from the drop-tube and sieved into the following size fractions;  $\geq 850 \mu\text{m}$ ,  $850 - 500 \mu\text{m}$ ,  $500 - 300 \mu\text{m}$ ,  $300 - 212 \mu\text{m}$ ,  $212 - 150 \mu\text{m}$ ,  $150 - 106 \mu\text{m}$ ,  $106 - 75 \mu\text{m}$ ,  $75 - 53 \mu\text{m}$ ,  $53 - 38 \mu\text{m}$  and  $\leq 38 \mu\text{m}$ . The sieved particles were mounted in transopic resin and prepared for microstructural analysis using OM and SEM according to the same protocol as described above for the ingot material. Samples were etched in a mixture of 5 ml  $\text{HNO}_3$  + 5ml  $\text{HCl}$  + 5 ml  $\text{HF}$  for microstructural analysis.

In addition to microstructural analysis using OM and SEM, selected area diffraction analysis in the transmission electron microscopy (TEM), using an FEI Tecnai TF20, was used to distinguish between the ordered and disordered variants of the  $\beta\text{-Ni}_3\text{Ge}$  phase. Samples were prepared for TEM analysis using an FEI Nova 200 Nanolab focused ion beam (FIB), with the sections cut being approximately  $10 \mu\text{m} \times 7 \mu\text{m}$  and between 55-70 nm in thickness. An example of a FIB milled section is shown in Figure 3.

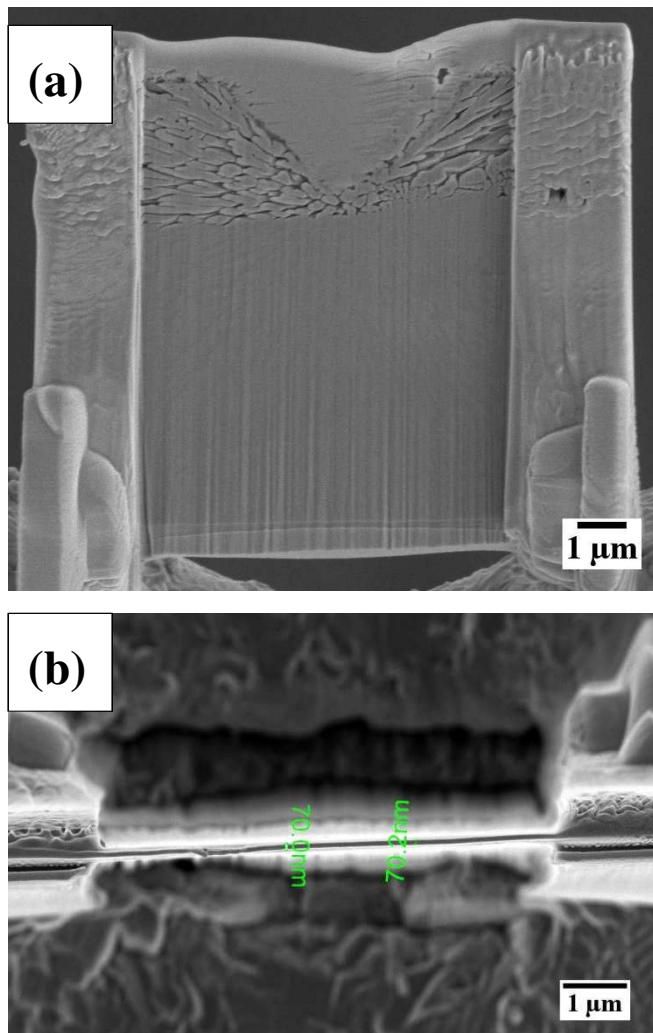


**Figure 3:** Preparation of a TEM sample by FIB milling of a sample mounted and polished for SEM analysis. Part of a spherulite structure can be seen at the top of the FIB cut section. The resulting FIB milling is shown a) in plan and b) cross sectional view.

## Results

The cooling rate for droplets produced during drop-tube processing is dependent principally upon the ratio of surface area to volume of the droplet. Consequently, a spray containing a wide range of particle sizes will produce droplets with a correspondingly wide range of cooling rates. Using the method described in [15], the cooling rate has been estimated as a function of droplet diameter and is shown in Figure 4. The only difference between the method employed by [15] and the calculation performed here is that [15] estimated the cooling rate in the liquidus-solidus interval, whereas for a congruently melting compound the sample will be isothermal during freezing. Therefore, we have calculated the cooling rate just after the completion of solidification. However, as the key parameter in the retention of disordered material and the nature of any APD's formed is the post-recalence cooling rate this is the most appropriate indicator of microstructural development. On this basis the range of cooling rates experienced by the droplets in these experiments spans the range 700 – 42,000 K s<sup>-1</sup> (corresponding to 850 μm and 53 μm droplets respectively).

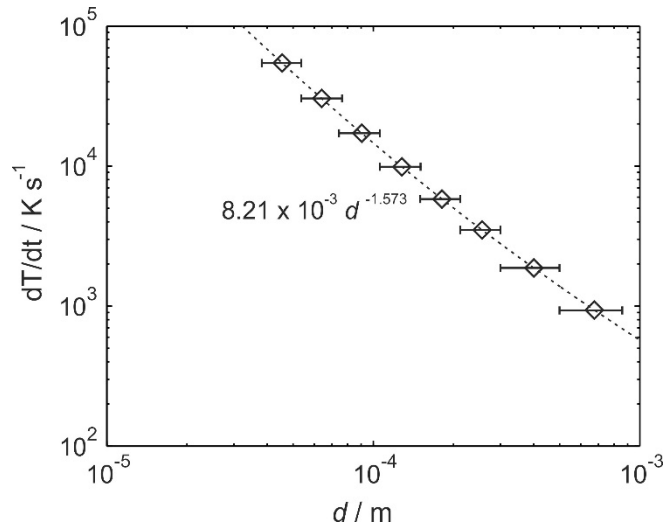


**Figure 4:** Estimate cooling rate for drop-tube processed Ni<sub>3</sub>Ge powder as a function of particle diameter.

The starting material for the drop-tube experiments was single phase  $\beta$ -Ni<sub>3</sub>Ge, this being confirmed by XRD analysis on the polished surface of the arc-melted ingot. It can be seen from Figure 5 that all the XRD peaks may be reliably indexed to the  $\beta$ -Ni<sub>3</sub>Ge phase using the ICDD reference pattern 04-004-3112. When similar material was deeply undercooled by Ahmad *et al.* using a melt fluxing technique, the resultant material remained single phase  $\beta$ -Ni<sub>3</sub>Ge [10]. XRD analysis reveals that the same is true during rapid cooling via drop-tube processing, with the drop-tube powders (diameter 850  $\mu$ m - 150  $\mu$ m) displaying peaks that can unambiguously be associated with the Ni<sub>3</sub>Ge reference pattern (see Figure 5).

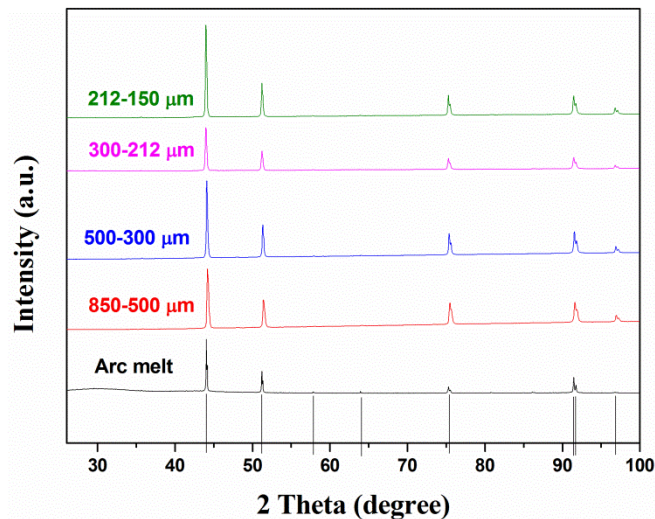


**Figure 5:** X-Ray diffraction analysis of an arc melted sample prior to drop-tube process (black) and drop-tube processed powders of 850-500  $\mu$ m (red), 500-300  $\mu$ m (blue), 300-212  $\mu$ m (pink) and 212-150  $\mu$ m (green) respectively. Vertical black lines indicate peak positions for the  $\beta$ -Ni<sub>3</sub>Ge reference pattern.

Figure 6 shows an SEM micrograph of a polished and etched sample from the 850-500  $\mu\text{m}$  sieve fraction. Numerous spherulite like structures, typically with diameters of the order of 10-20  $\mu\text{m}$ , are evident in an otherwise featureless matrix. Such structures are very rare in metallic systems, although appear to be ubiquitous throughout the drop-tube powders in this size fraction and also in the 500-300  $\mu\text{m}$  size fraction. In the smaller diameter powders the spherulite diameter is correspondingly reduced, typically to < 10  $\mu\text{m}$ , but their volume fraction is increased. Spherulites are also observed in the 300-212  $\mu\text{m}$  size fraction, although these features are now small (typically 3  $\mu\text{m}$  or less) and co-exist with dendritic structures.

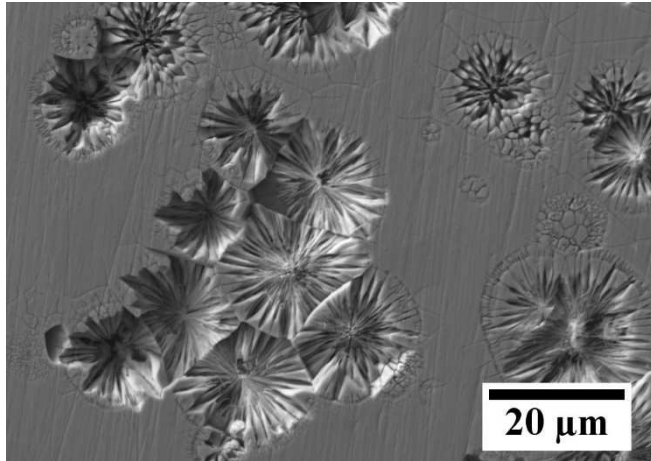


**Figure 6:** SEM micrograph of an HF etched  $\beta\text{-Ni}_3\text{Ge}$  drop-tube particle from the 850 – 500  $\mu\text{m}$  size fraction. Numerous spherulite structures are clearly evident in a more-or-less featureless matrix.

With a yet further reduction in the powder size to 212-150  $\mu\text{m}$ , spherulites cease to be observed in the microstructure of the etched droplets, with dendrites becoming the dominant structure. An example of this is shown in Figure 7. Dendrites continue to be the dominant morphology evident in the drop-tube powders as the particle size is reduced to 75  $\mu\text{m}$ . However, while the morphology in the 150-106  $\mu\text{m}$  sieve fraction resembles that in the 212-150  $\mu\text{m}$  fraction, with dendrites displaying well-developed orthogonal side-branches, in the 106-75  $\mu\text{m}$  sieve fraction the dendrites in some droplets take on a different character. In particular, while many of the droplets still display morphologies similar to that in Figure 7, in some of the droplets (Figure 8) the side-branches are no longer orthogonal to the main trunk and may also be subject to irregular splitting as if taking on a doublon type character. With reference to Figure 8 we note that for the dendrite marked (i), towards the top of the droplet as pictured, the angle between the primary trunk and the secondary arms is close to  $60^\circ$ . Conversely, for the dendrite marked (ii), close to the centre of the droplet, the angle between the primary trunk and the longer part of the secondary arms is close to  $45^\circ$ , while for the smaller branches, emanating near the root of each secondary arm, the angle is close to  $30^\circ$ . Typically, the observation of a switch from orthogonal, to non-orthogonal, side-branching in a cubic system is indicative of a switch in the growth direction, from  $\langle 100 \rangle$  close to equilibrium, to either  $\langle 110 \rangle$  or  $\langle 111 \rangle$  with increasing departure from equilibrium. A number of systems have been reported to show such transitions [16, 17]. We also note the clear

curvature in the primary trunk of the dendrite marked (ii), which may be due to some anomaly of the heat flow within the droplet during solidification.

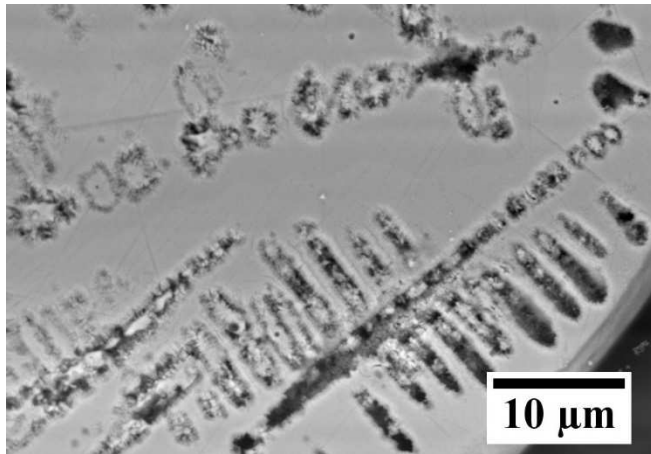


**Figure 7:** SEM micrograph of an HF etched  $\beta$ -Ni<sub>3</sub>Ge drop-tube particle from the 212 – 150  $\mu\text{m}$  size fraction showing dendritic structures in a featureless matrix.

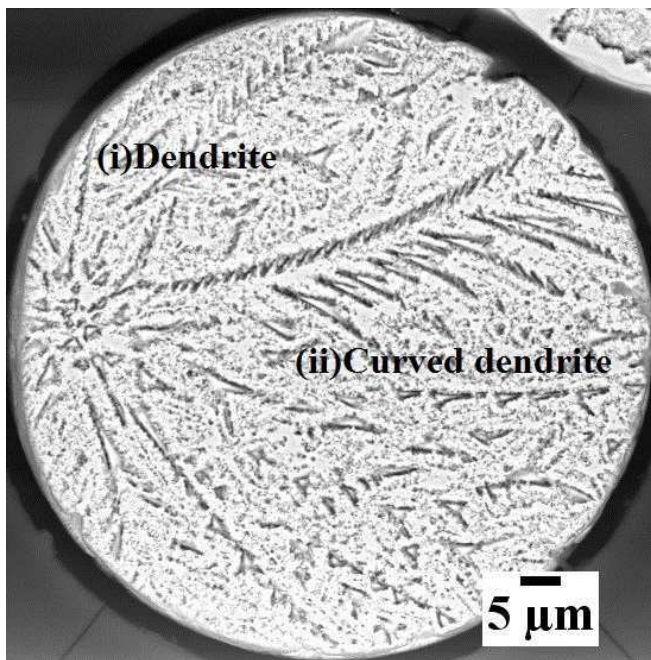


**Figure 8:** SEM micrograph of an HF etched  $\beta$ -Ni<sub>3</sub>Ge drop-tube particle from the 106 – 75  $\mu\text{m}$  size fraction, showing dendritic structure with non-orthogonal side-branching. Two dendrites in particular are indicated with side-branches at angles of (i) 60° and (ii) 45° and 30°.

Finally, in the smallest size fraction investigated as part of this study, yet another structure is observed, which we might describe as being of the ‘dense branched fractal’ or ‘dendritic seaweed’ type, an example of which is shown in Figure 9 for the 53 – 38  $\mu\text{m}$  size fraction.

We note, in particular with respect of Figure 7, that the dendrites appear to be spatially isolated from each other and embedded within a featureless matrix. Such microstructures are not normally characteristic of fully crystalline materials, where interpenetration of differently oriented dendrites tends to produce a complex as-solidified microstructure. Indeed, the morphology shown in Figure 7 is more typical of the growth of crystalline dendrites during partial devitrification of an amorphous matrix. This is also one of the habitats in which spherulites are most commonly observed, although XRD analysis shows no indication of the broad humps typical of the presence of an amorphous phase. Consequently, in order to understand the mechanism giving rise to these structures we have turned to TEM, with selected area diffraction patterns being obtained for the spherulitic, dendritic and matrix phases.

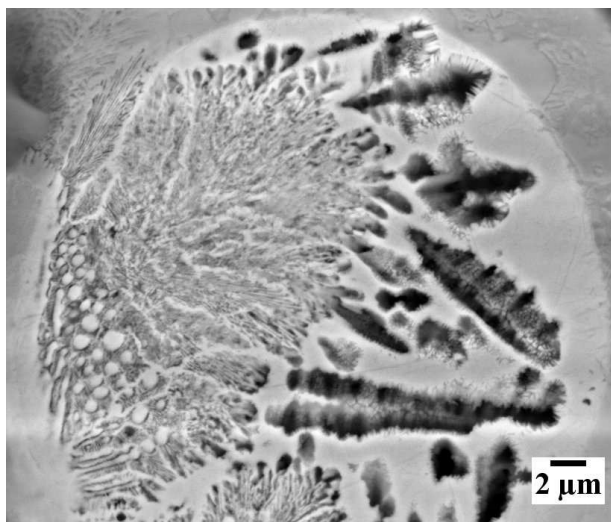


**Figure 9:** SEM micrograph of an HF etched  $\beta$ -Ni<sub>3</sub>Ge drop-tube particle from the 53 – 38  $\mu\text{m}$  size fraction showing dense branched fractal or ‘dendritic seaweed’ structure.

Figure 10a shows a TEM bright field image of a FIB section through a spherulite and some of the immediately surrounding matrix material. Two regions, labelled (i) matrix materials well away from the spherulite and (ii) inside the spherulite, are shown on the figure and indicate the locations from which selected area diffraction patterns have been taken. The selected area diffraction patterns from regions (i) and (ii) are shown in Figure 10 b-c respectively, from which it can be established that both patterns share a set of common points corresponding to an fcc crystal structure. However, Figure 10a (region i) also displays superlattice spots corresponding to the L1<sub>2</sub> ordered fcc structure. Broadly similar results are obtained from a FIB section cut from a particle in the 212 – 150  $\mu\text{m}$  sieve fraction, including a dendritic and matrix region. The TEM bright field image for the slice is shown in Figure 11a, with again two regions indicated corresponding (i) matrix materials well away from the dendrite and (ii) inside the dendritic region. As with the spherulitic slice, the selected area diffraction pattern taken from the matrix region (Figure 11b) shows clear superlattice spots which, correspondingly, are absent from the selected area diffraction pattern taken from the centre of the dendritic region (Figure 11c).

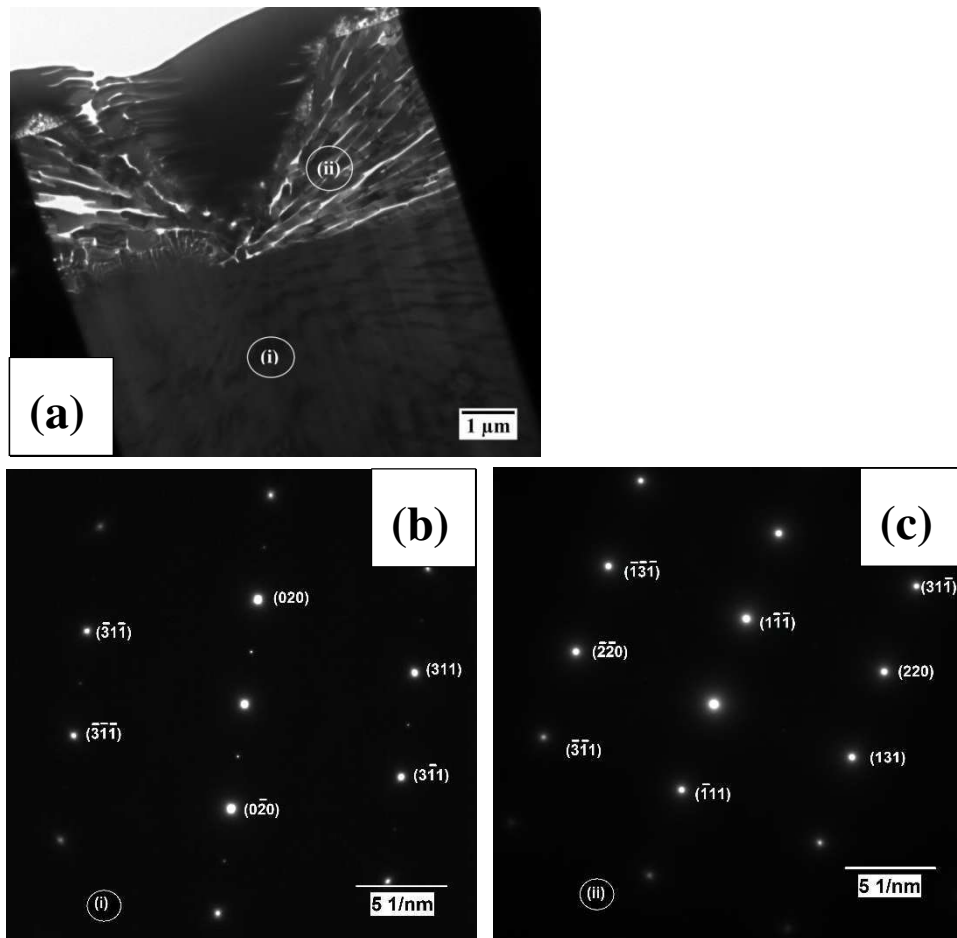


**Figure 10:** (a) TEM bright field image of a spherulite and surrounding matrix material in a 850 – 500 μm particle, (b and c) selected area diffraction patterns from regions i and ii identified in the bright field image (i) matrix materials well away from the spherulite, (ii) inside the spherulite

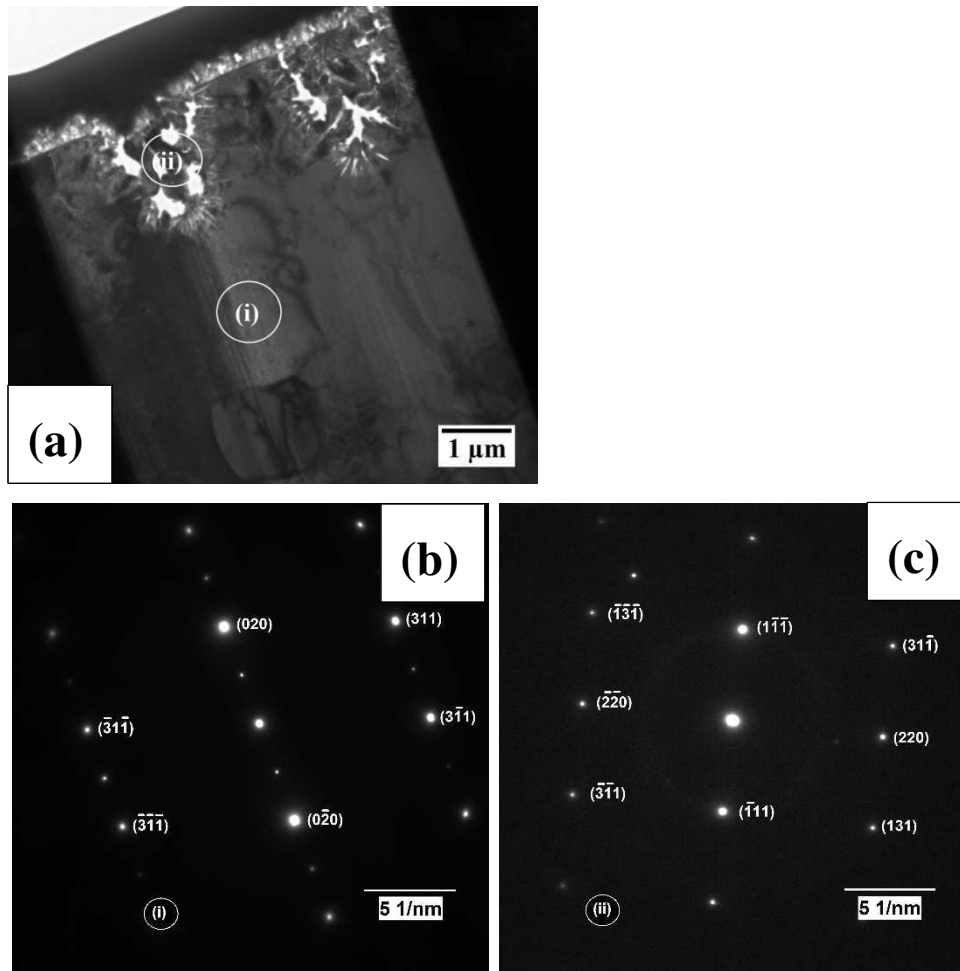


**Figure 11:** (a) TEM bright field image of a dendrite and surrounding matrix material in a 212 -150 μm particle, (b and c) selected area diffraction patterns from regions i and ii identified in the bright field image (i) matrix materials well away from the dendrite and (ii) inside the dendrite.

## Discussion

From the SEM, TEM and XRD data presented a consistent picture of the solidification dynamics of this material emerges. We believe that all samples are single phase  $\beta$ -Ni<sub>3</sub>Ge, with the various morphologies (spherulitic, dendritic and fractal) revealed during etching to be the disordered variant of this phase while the ‘featureless’ matrix material is the more normally encountered, chemically ordered variant. This would be consistent with the TEM results in which superlattice spots are observed in the matrix material but not in the spherulites or dendrites. Whether the matrix material genuinely is featureless, or not, is not clear, it may just be resistant to the etch used. In this respect we note that the etch used here (equal parts HF, HCl and HNO<sub>3</sub>) is one of the more aggressive etchants used in metallography, although this would be consistent with the chemically resistant nature of intermetallic compounds. We postulate therefore that the spherulites and dendrites were the rapid solidification morphologies that grew during recalescence and that the ‘featureless’

matrix grew more slowly during the post-recalescence period. This would also be consistent with the observation that the volume fraction of spherulites/dendrites tends to increase with decreasing particle size (increasing cooling rate).

However, two features of the microstructures observed are really quite surprising. The first is that disordered material is retained in even the largest droplets, wherein cooling rates are of the order of  $\sim 700 \text{ K s}^{-1}$ . Typically much higher cooling rates would be expected to be required to inhibit reordering [5], indicating that the ordering kinetics in  $\beta\text{-Ni}_3\text{Ge}$  are probably quite slow. This would be consistent with the low critical velocity,  $V_C$ , observed by [10] for the onset of fully disordered growth in  $\beta\text{-Ni}_3\text{Ge}$ , relative to other ordered intermetallics such as Fe-18 at. % Ge and CoSi,  $V_C$  being proportional to the characteristic velocity for interface diffusivity. A corollary of this is that in the absence of reordering, no APD's have been observed in any size fraction of droplets. The second surprising feature of the microstructure is the occurrence of the disordered material in the form of spherulites.

The crystalline morphology termed spherulitic was first observed by Talbot in 1837 during the crystallisation of borax from phosphoric acid [18]. These non-equilibrium structures are observed in small molecule organic crystals, together with some minerals, volcanic rocks, inorganic crystals and a few pure elements (e.g. graphite, sulphur and selenium) [19]. Spherulites are only rarely observed during the solidification metals, generally in eutectic structures such as graphite formations in cast irons [20] and eutectic carbides in tool steels [21]. However, it is in polymers, particularly those of high molecular weight, where spherulites are most common. In polymers, spherulites are typically not eutectic, but are crystalline-amorphous composite structures consisting of multiply branched crystalline arms separated by amorphous regions between the arms [19], with spherulite growth normally being explained by topological constraints restricting the reorientation of the long chain molecules during crystallization.

Spherulite growth is also observed in metallic glass systems during devitrification in the solid state. Amorphous metallic systems that display spherulite structures include Fe-B [22], Fe-Si-B [23], Zr-Cu-Al [24] and Zr-Cu-Ni-Al-Nb [25]. In some cases the spherulites have the typical eutectic structure of metallic spherulites formed from the melt (e.g.[22]), in others this is not so. In Fe-Si-B, [23] identified the spherulites as being pure Fe, while in Zr-Cu-Al [24] identified the spherulites as being a previously unknown, single-phase material, with the  $\text{Pcm}_2$  (or possibly  $\text{Pcma}$  or  $\text{Pmma}$ ) space group.

Although there is controversy in the literature as to the formation mechanism for spherulitic growth, a number of common requirements for their formation have been identified. One is a tendency towards non-crystallographic, small angle branching [26]. A second is a high viscosity in the medium being crystallised. The importance of this has been demonstrated unambiguously by Morse *et al.* [27, 28] who, in a study of the crystallisation behaviour of inorganic salts, identified around 70 salts that would crystallise in spherulitic form if grown in a gel, but not otherwise. As with polymers, the spherulite morphology observed by Morse *et al.* was that of a single phase of the salt being precipitated, not a eutectic.

While in some respects crystallization from a metallic glass precursor is similar to crystallization from the melt, in other respects it is quite different. The main difference is that

the viscosity of a glass is much higher than that of a melt and, correspondingly, the atomic diffusivity is much lower in a glass, compared to a melt of the equivalent composition. Consequently, crystallization from a glass can, but is not always, restricted to short range diffusion. This in turn means that growth kinetics dominate over diffusion. As it is diffusion that gives rise to dendrites, the parabolic shape of the dendrite tip being the most efficient morphology for transporting solute away from the growing solid, crystallisation to a spherulitic morphology is the natural consequence of kinetically limited growth. Sun & Flores [25] argue that under pure kinetically limited growth, an isotropic material would grow as a perfect sphere but that competition with crystalline anisotropy gives rise to different crystal orientations within the growing sphere, resulting in the fine needle spherulite morphology.

An analogous situation may be considered to exist in the growth of  $\beta$ -Ni<sub>3</sub>Ge from its parent melt. As the compound is congruently melting there is no requirement for long range solute transport by diffusion. This is consistent with EDX measurements which show that, to within experimental uncertainty, the chemical composition within the spherulite and dendrite morphologies is identical to that of the surrounding matrix material. With regard to spherulite growth we postulate that thermal transport within these large particles is probably sufficiently fast that the droplet approximates the conditions of isothermal solidification. Under these conditions kinetics dominate, with the kinetically favoured fine needle spherulite morphology resulting.

Dendritic morphologies are first observed in the 300-212  $\mu\text{m}$  sieve fraction (cooling rate  $> 2500 \text{ K s}^{-1}$ ) and become the dominant morphology for particles with diameter  $< 212 \mu\text{m}$  (cooling rate  $> 4500 \text{ K s}^{-1}$ ). A well-documented (see e.g. Lee & Ahn [29]) feature of droplet solidification by techniques such as drop-tube processing or gas atomization is that increased cooling rate, together with the melt sub-division effect, leads to rapidly increasing undercooling within the droplet as the droplet size decreases. We postulate that with increasing undercooling the growth rate will increase and the need for efficient diffusion of heat from the growing solid results in thermal dendrites being formed, that is dendrites are formed due to the destabilisation of the solid-liquid interface by growth into a negative temperature gradient.

It is not clear whether this transition to dendritic growth also coincides with any other transition in the growth mechanism. However, the most natural assumption would be to associate the switch in growth morphology from the spherulitic to dendritic growth morphology with the transition to fully disordered growth observed by Ahmad *et al.* [10] at an undercooling of 168 K. A corollary of this would be that the observed spherulitic structures are only partially disordered, with the spherulite structure being an ordered-disordered composite. This might be considered as an analogue of the crystalline-amorphous type of spherulites observed in polymers, rather than the eutectic type more common in metals grown from their parent melt. The residual ordering in these structures would account for the low growth velocity observed by [10] at low undercooling. In line with most materials we may assume that it is normal capillary anisotropy that gives rise to the directionality observed in the dendritic structures.

Finally, in the smallest droplets, wherein cooling rates may approach  $40,000 \text{ K s}^{-1}$ , we observe a dense branched fractal morphology. Such structures, which are not unusual at very large departures from equilibrium [30, 31] are indicative of the loss of directionality during growth, either due to a weakening of the strength of the crystalline anisotropy at high growth velocity or due to a competition between differently directed capillary and kinetic anisotropies [32]. The somewhat irregular or distorted dendritic morphology apparent in Figure 8 is likely to also be a consequence of this loss of directionality, with such morphologies having previously been observed at undercoolings just below those which give rise fully to 'dendritic seaweed' morphologies [17, 31].

## Summary & Conclusion

Rapid solidification of the congruently melting intermetallic compound  $\text{Ni}_3\text{Ge}$  has revealed a range of solidification microstructures, which with increasing departure from equilibrium are

- 1) spherulites,
- 2) dendrites,
- 3) distorted dendrites,
- 4) dense-branched fractal morphology.

All of these morphologies appear to be composed of the same chemically disordered form of the  $\text{Ni}_3\text{Ge}$  compound, embedded in a matrix of the ordered variant of the same compound. It is postulated that the disordered form grew during recalescence, the ordered matrix post-recalescence. All of the morphologies can be explained by the interplay of diffusion, capillarity and kinetics. In the absence of solute partitioning, spherulites grow as a diffusionless, kinetically dominated microstructure. At higher cooling rates/growth velocities the negative temperature gradient ahead of the growing solid-liquid interface results in thermal dendrites. At yet higher growth velocity, capillary and kinetic anisotropies come into competition leading to a change in the dendrite growth direction, irregular dendrite growth and ultimately a dense-branched fractal morphology. Although each these morphologies have been observed in various metallic systems at different undercoolings, it is extremely unusual to observe the entire range of morphologies in a single material. As such, further study of  $\beta\text{-Ni}_3\text{Ge}$  may yield important information about both the growth of spherulites in metals and the transition between the dendrite to dense-branched fractal growth morphologies.

## References

- [1] R. Cahn, P. Siemers, J. Geiger, P. Bardhan, The order-disorder transformation in  $\text{Ni}_3\text{Al}$  and  $\text{Ni}_3\text{Al-Fe}$  alloys—I. Determination of the transition temperatures and their relation to ductility, *Acta Metallurgica*, 35 (1987) 2737-2751.
- [2] A. Inoue, H. Tomioka, T. Masumoto, Microstructure and mechanical properties of rapidly quenched  $\text{L}_{12}$  alloys in Ni-Al-X systems, *Metallurgical Transactions A*, 14 (1983) 1367-1377.

- [3] H. Assadi, M. Barth, A. Greer, D.M. Herlach, Microstructural development in undercooled and quenched Ni<sub>3</sub>Al droplets, in: *Materials Science Forum*, Trans Tech Publ, 1996, pp. 37-44.
- [4] P. Haasen, *Physical Metallurgy*, Cambridge University Press, Cambridge, 1978.
- [5] A. Greer, H. Assadi, Rapid solidification of intermetallic compounds, *Materials Science and Engineering: A*, 226 (1997) 133-141.
- [6] J. Baker, J. Gahn, Solute trapping by rapid solidification, *Acta Metallurgica*, 17 (1969) 575-578.
- [7] W. Boettinger, M. Aziz, Theory for the trapping of disorder and solute in intermetallic phases by rapid solidification, *Acta Metallurgica*, 37 (1989) 3379-3391.
- [8] S. Reutzel, H. Hartmann, P. Galenko, S. Schneider, D. Herlach, Change of the kinetics of solidification and microstructure formation induced by convection in the Ni–Al system, *Applied Physics Letters*, 91 (2007) 041913.
- [9] D.M. Herlach, Metastable materials solidified from undercooled melts, *Journal of Physics: Condensed Matter*, 13 (2001) 7737.
- [10] R. Ahmad, R. Cochrane, A. Mullis, Disorder trapping during the solidification of  $\beta$ -Ni<sub>3</sub>Ge from its deeply undercooled melt, *Journal of Materials Science*, 47 (2012) 2411-2420.
- [11] K. Biswas, G. Phanikumar, D. Holland-Moritz, D.M. Herlach, K. Chattopadhyay, Disorder trapping and grain refinement during solidification of undercooled Fe–18 at.% Ge melts, *Philosophical Magazine*, 87 (2007) 3817-3837.
- [12] R. Ahmad, R. Cochrane, A. Mullis, The formation of regular  $\alpha$ Ni- $\gamma$  (Ni<sub>3</sub>1Si<sub>12</sub>) eutectic structures from undercooled Ni–25 at.% Si melts, *Intermetallics*, 22 (2012) 55-61.
- [13] L. Cao, R.F. Cochrane, A.M. Mullis, Microstructural Evolution and Phase Formation in Rapidly Solidified Ni-25.3 at.% Si Alloy, *Metallurgical and Materials Transactions A*, 46 (2015) 4705-4715.
- [14] A. Nash, P. Nash, *Binary Alloy Phase Diagrams*, in: US National Bureau of Standards Monograph Series 25, Elsevier, ASM, Ohio, 1976, pp. 35.
- [15] O. Oloyede, T.D. Bigg, R.F. Cochrane, A.M. Mullis, Microstructure evolution and mechanical properties of drop-tube processed, rapidly solidified grey cast iron, *Materials Science and Engineering: A*, 654 (2016) 143-150.
- [16] K. Dragnevski, R. Cochrane, A. Mullis, The solidification of undercooled melts via twinned dendritic growth, *Metallurgical and Materials Transactions A*, 35 (2004) 3211-3220.
- [17] E.G. Castle, A.M. Mullis, R.F. Cochrane, Evidence for an extensive, undercooling-mediated transition in growth orientation, and novel dendritic seaweed microstructures in Cu–8.9 wt.% Ni, *Acta Materialia*, 66 (2014) 378-387.
- [18] W.H.F. Talbot, *Phil. Trans. R. Soc. London*, London, 1837.
- [19] J. Magill, Review spherulites: A personal perspective, *Journal of Materials Science*, 36 (2001) 3143-3164.
- [20] T.T. Li, X.N. Pan, H.L. Zheng, X.L. Tian, Calculation of carbon diffusion coefficient in spheroidal graphite cast iron, in: X.H. Liu, Z.H. Bai, Y.H. Shuang, C.L. Zhou, J. Shao (Eds.) *Applied Mechanics and Materials*, Vol. 217-219, 2012, pp. 476-482.

- [21] M. Kusy, L. Caplovic, P. Grgac, A. Vyrostkova, Solidification microstructures in the rapidly solidified powder of high alloyed V-Cr tool steel, *Journal of Materials Processing Technology*, 157 (2002) 729-734.
- [22] A. Deriu, F. Malizia, F. Ronconi, M. VittoriAntisari, S.M. King, Microstructural characterization of Fe<sub>80</sub>B<sub>20</sub> eutectic spherulites by small-angle neutron scattering and transmission electron microscopy, *Journal of Applied Physics*, 79 (1996) 2296-2301.
- [23] K. Chrissafis, M. Maragakis, K. Efthimiadis, E. Polychroniadis, Detailed study of the crystallization behaviour of the metallic glass Fe<sub>75</sub>Si<sub>9</sub>B<sub>16</sub>, *Journal of Alloys and Compounds*, 386 (2005) 165-173.
- [24] T. Yano, Y. Yorikado, Y. Akeno, F. Hori, Y. Yokoyama, A. Iwase, A. Inoue, T.J. Konno, Relaxation and crystallization behavior of the Zr<sub>50</sub>Cu<sub>40</sub>Al<sub>10</sub> metallic glass, *Materials Transactions*, 46 (2005) 2886-2892.
- [25] H. Sun, K.M. Flores, Spherulitic crystallization behavior of a metallic glass at high heating rates, *Intermetallics*, 19 (2011) 1538-1545.
- [26] H. Keith, F. Padden Jr, A phenomenological theory of spherulitic crystallization, *Journal of Applied Physics*, 34 (1963) 2409-2421.
- [27] H.W. Morse, C.H. Warren, J.D.H. Donnay, Artificial spherulites and related aggregates, *American Journal of Science*, (1932) 421-439.
- [28] H. Morse, J. Donnay, Optics and structure of three-dimensional spherulites, *American Mineralogist*, 21 (1936) 391-427.
- [29] E.S. Lee, S. Ahn, Solidification progress and heat transfer analysis of gas-atomized alloy droplets during spray forming, *Acta Metallurgica et Materiala*, 42 (1994) 3231-3243.
- [30] K. Dragnevski, R. Cochrane, A. Mullis, Experimental evidence for dendrite tip splitting in deeply undercooled, ultrahigh purity Cu, *Physical Review Letters*, 89 (2002) 215502.
- [31] E.G. Castle, A.M. Mullis, R.F. Cochrane, Mechanism selection for spontaneous grain refinement in undercooled metallic melts, *Acta Materialia*, 77 (2014) 76-84.
- [32] J. Dantzig, P. Di Napoli, J. Friedli, M. Rappaz, Dendritic Growth Morphologies in Al-Zn Alloys—Part II: Phase-Field Computations, *Metallurgical and Materials Transactions A*, 44 (2013) 5532-5543.